ACS APPLIED MATERIALS & INTERFACES

Research Article

www.acsami.org

Trace Amounts of Water-Induced Distinct Growth Behaviors of NiO Nanostructures on Graphene in CO_2-Expanded Ethanol and Their Applications in Lithium-Ion Batteries

Linhai Zhuo,[†] Yingqiang Wu,[†] Wei Zhou,[‡] Lingyan Wang,[†] Yancun Yu,[†] Xinbo Zhang,*[,‡] and Fengyu Zhao*[,†]

[†]State Key Laboratory of Electroanalytical Chemistry, Changchun Institute of Applied Chemistry, and [‡]State Key Laboratory of Rare Earth Resource Utilizations, Changchun Institute of Applied Chemistry, Chinese Academy of Sciences, Changchun 130022, P.R. China

Supporting Information

ABSTRACT: In this work, we have developed a new method to grow NiO nanomaterials on the surface of graphene nanosheets (GNSs). The morphologies of NiO nanomaterials grown on GNSs could be tailored by trace amounts of water introduced into the mixed solvents of CO_2-expanded ethanol (CE). Small and uniform Ni-salt nanoparticles (Ni-salt-NPs) were grown on the surface of graphene oxide (GO) through the decomposition of nickel nitrate directly in CE. However, when trace amounts of water were introduced into the mixed solvents, Ni-salt nanoflakes arrays (Ni-salt-NFAs) were grown on the surface of GO with almost perpendicular direction. After thermal treatment in N_2 atmosphere, these Ni-salt @GO composites were converted to NiO@GNSs composites. The forming mechanisms of the NiO-NPs@GNSs and NiO-NFAs@GNSs were discussed by series comparative experiments. The presence of the trace amounts of water affected the chemical composition and structure of the precursors formed in CE and the growth behaviors on the surface of GNSs. When used as anode materials for lithium-ion batteries, the NiO-NPs@GNSs composite exhibited better cycle and rate performance compared with the NiO-NFAs@GNSs.

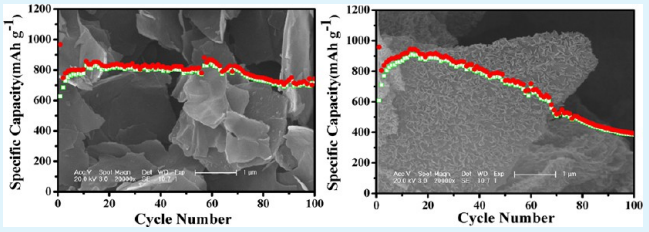

KEYWORDS: *CO_2-expanded ethanol, NiO nanostructures, growth behaviors, anode material, lithium-ion batteries*

1. INTRODUCTION

Graphene nanosheet (GNS), because of its excellent electronic conductivity, mechanical properties, and high surface area (theoretical value of 2630 m^2 g^{-1}), has become an ideal substrate to immobilize functional materials for different high-performance energy storage devices.[1−7] The presence of GNSs in the GNS-based composites can supply a conducting and well-accessible carbon network, which affords facile electron transport to ensure the guest component electrochemically active.[8,9] In addition to their good conductivity, the high surface areas can supply enough growth sites to immobilize the guest components and prevent them aggregation in the composites.[10,11] Furthermore, the good mechanical flexibility of GNSs can readily absorb the massive volume expansion associated with a conversion reaction electrode, which is crucial for cyclability of electrodes.[12−14]

Although many metal oxide@GNSs composites have been reported recently, most of the active components are simple zero-dimensional (0D) nanoparticles.[10,15−19] In recent years, materials with other morphologies such as 1D and 2D nanomaterial growing on GNSs have also been reported.[1,3,20−26] But only several examples have demonstrated the growth behaviors and the mechanisms of these 1D and 2D nanomaterials on GNSs. For example, Chen et al. reported the synthesis of MnO_2 nanoneedles@GO and the formation mechanisms.[24] Wang et al. reported that the morphologies of some oxides nanocrystals could be controlled by tuning the degree of oxidation of the GNSs.[1] Ding et al. also reported that the addition of mercaptoacetic acid in the process of synthesis could lead to SnO_2 nanoflake arrays growing on GNSs.[15] Therefore, it is still a challenge to control the morphologies of nanocrystals to grow on GNSs and realize their growth behaviors.

Most of the metal oxide@GNSs composites were usually synthesized by a solution-based chemical synthesis method. The commonly used solvents such as ethanol and water are of high viscosity, surface tension and low diffusivity.[27,28] These properties strongly limit the ability of solvents to homogenously disperse and smoothly transfer of the generated solid intermediates to grow on the surface of substrate, resulted in the poor adherent of guest components on substrate or crystallize and aggregate in solution, which made the investigation of the growth behaviors more difficulty.[1,3,29] As a green or sustainable technology, supercritical fluid (SCF) has

Received: April 15, 2013
Accepted: July 11, 2013
Published: July 11, 2013

drawn sustaining interest both in the current scientific and industrial fields.[27,30] SCF is an attractive alternative to conventional solvents due to its unique features of tunable physical properties characterized with low viscosity, high diffusivity, and absence of surface tension. These properties make SCF to be a potentially superior solvent for the synthesis and processing of nanomaterials (nanoscale particles, wires, and films).[30] The most widely studied SCF is supercritical carbon dioxide ($scCO_2$) because it is nonflammable, essentially nontoxic, inexpensive, and environmentally benign. Recently, the specific properties of $scCO_2$ have been exploited for synthesizing of functional nanomaterials, especially in the field of inorganic and hybrid materials.[29,31,32] The materials could assemble according to their wills in SCF because it can avoid the effect of viscosity, surface tension, and diffusivity generated from some routine solvents. So, the growth mechanisms could be revealed easily in SCF because the effects originating from solvents have been avoided.

Nickel oxide (NiO) has long been investigated as one of the most promising materials for lithium-ion batteries (LIBs) or capacitor because of its abundance and low cost.[8,33−45] However, the cycle ability of pure NiO is poor because of its unsatisfactory electronic conductivity and the volume expansion after repetitive charging and discharging, which causes the collapse of the active materials and the loss of electrical contact. To circumvent this problem, GNSs have been used as additive for NiO anodes to improve their lithium-ion storage properties.[8,10,23,34,36,41,46] In this work, NiO was used as a model material for investigating the growth behavior on the surface of GNSs. The morphologies of NiO growing on GNSs could be controlled by adding trace amounts of water to the mixed solvents of CO_2-expanded ethanol (CE). Small and uniform Ni-salt nanoparticles were grown on the surfaces of graphene oxide (GO) through the decomposition of nickel nitrate in CE. However, when trace amounts of water was introduced in the mixed solvents, Ni-salt nanoflake arrays were formed on the surface of GO. After thermal treatment in N_2 atmosphere, these Ni-salt@GO composites were converted to NiO@GNSs composites. The formation mechanisms of the NiO nanoparticles@GNSs (NiO-NPs@GNSs) and NiO nanoflake arrays@GNSs (NiO-NFAs@GNSs) have been investigated by series comparative experiments. When applied as the anode materials for LIBs, the NiO-NPs@GNSs manifested better cyclability and rate capability than the NiO-NFAs@GNSs, suggesting that the electrochemical performances of these composites was depended on the morphology of the NiO nanocrystals growing on GNSs. The NiO-NPs@GNSs nanocomposite showed good cyclability with a specific revisable capacity of 741.5 mA h g^{-1} at a charge−discharge rate of 100 mA g^{-1} at the 100th cycle. Even at a high current density of 4 A g^{-1}, the NiO-NPs@GNSs also presented good rate performance. In contrast, the NiO-NFAs@GNSs showed inferior performance compared to the NiO-NPs@GNSs nanocomposite.

2. EXPERIMENTAL SECTION

2.1. Materials. All chemicals were used as received without further purification. $Ni(NO_3)_2{\cdot}6H_2O$ was purchased from Beijing Chemical Works. Natural graphite powder was purchased from Shanghai Colloid Chemical Plant.

2.2. Synthesis of NiO@GNSs Composites. GO was prepared from purified natural graphite powder according to the improved method.[31] GO (25 mg) was diluted in absolute alcohol (10 mL), ultrasonication for 120 min. One-tenth of a gram of $Ni(NO_3)_2{\cdot}6H_2O$ was added to the flask. Then the dispersion was loaded into a high-pressure 50 mL vessel, which subsequently was placed into an oil bath at 150 °C and pumped CO_2 to form a homogeneous expanded fluid (12.0 MPa) under rapid stirring. The reactor was heated to the reaction temperature of 200 °C for 2 h. After it was cooled to ambient temperature, the vessel was slowly depressurized. The precursor (Ni-salt-NPs@GO composite) was collected though centrifugation and dried in vacuum at 100 °C for 6 h. Then, the precursor was calcined in a tube furnace at 400 °C for 3 h with a heating rate of 3 °C min^{-1} under a N_2 atmosphere flow in which the Ni-salt NPs were decomposed to NiO in situ and to form the NiO-NPs@GNSs. The Ni-salt nanoflake arrays growing on GO (Ni-salt-NFAs@GO) and NiO-NFAs@GNSs were also prepared by the same way, except that 40 μL of water was introduced to the reaction system. To investigate the growth mechanism, we also prepared the intermediate compounds without GO by the same method. The intermediate compound obtained in the CE without GO was designated as Ni-salt, whereas the other one obtained with additional trace amounts of water introduced in the mixed solvents was designated as Ni-salt-water.

2.3. Materials Characterizations. The phase structures were characterized with X-ray diffraction [XRD, Bruker D8 Advance diffractometer using Cu K_α (λ = 1.5418 A°)]. The morphology of the materials was analyzed by the scanning electron microscope (SEM Hitachi S-4800). Transmission electron microscope (TEM) was recorded on a Tecnai G2 operating at 200 kV for the detailed microstructure information of the sample. Thermal gravimetric analysis (TGA) was carried out using a TGA 2050 thermogravimetric analyzer. The existence of CO_3^{2-} and/or NO_3^- in resultant solid compounds was confirmed by CHN-analysis (VarioEL CHN). The chemical bond information was confirmed by Fourier transform infrared spectroscopy (FTIR) that recorded with Bruker Vertex 70 in the frequency range of 4000−450 cm^{-1}.

2.4. Electrochemical Measurements. The electrochemical tests were measured using two-electrode 2025-type coin cells assembled in an argon-filled glovebox. Lithium sheets served as the counter electrode and reference electrode, and a polypropylene film (Celgard-2300) was used as a separator. The electrolyte was a 1.0 M $LiPF_6$ solution in a mixture of EC-DMC (1:1 in volume). The working electrodes were prepared by a slurry coating procedure. The slurry consisted of 80 wt % active materials, 10 wt % acetylene black and 10 wt % polyvinylidene fluorides dissolved in *N*-methyl-2-pyrrolidinone. This slurry was spread on copper foil, which acted as a current collector. The electrodes were dried at 100 °C for 4 h in air, and then at 100 °C in a vacuum for another 12 h and pressed. The weight of every electrode was weighed accurately by electronic balance. The mass of the active materials was controlled in the range of 1−2 mg. Furthermore, the thickness of the electrode was measured by SEM. As can be seen from Figure S1 in the Supporting Information, the thickness of the active materials was about 16 μm at a mass of 1.82 mg. Galvanostatic charge−discharge cycles were carried out on a battery tester between 0.01 and 3.00 V at various current densities on a NEWARE cell test instrument (Shenzhen Neware Electronic Co., China).

3. RESULTS AND DISCUSSION

The structure and purity of the NiO-NPs@GNSs, NiO-NFAs@GNSs nanocomposites together with pure GNSs were characterized by XRD. As shown in Figure 1, the diffraction peaks at 25° for pure GNSs can be attributed to graphite-like (002) reflection. The peaks at 37.3, 43.4, and 63.0° of the two nanocomposites can be ascribed to NiO (JCPDS No. 78−0643).[37] Compared to the XRD pattern of pure NiO, an additional small and low broad diffraction peak appeared at about 25°, corresponding to the (002) diffraction peak of the disorderedly stacked GNSs.[23] These results suggest that the hybrid material is composed of GNSs and NiO. Because GNSs can be burned away while the bare NiO is stable in air at high

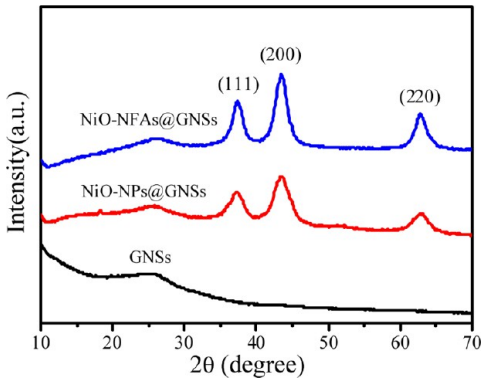

Figure 1. XRD patterns of the NiO-NPs@GNSs, NiO-NFAs@GNSs, and GNSs.

temperature. TGA analysis was carried out in air to quantify the amount of GNSs in the composites. TGA analysis for the composites was carried out in air to quantify the amounts of GNSs in the composites. As seen from Figure S2 in the Supporting Information, the weight loss over the temperature ranged from 40 to 200 °C might be due to the loss of residual water in the samples. The main weight loss at about 300−500 °C, was ascribed to the oxidation and decomposition of GNSs in air. According to the TGA analysis, the amounts of GNSs in these nanocomposites were about 31.5%.

To investigate the morphologies of the samples, SEM and TEM images were collected for the NiO-NPs@GNSs and NiO-NFAs@GNSs nanocomposites. As shown in Figure 2a, the SEM image of the NiO-NPs@GNSs showed that the two-dimensional GNSs were well decorated with a thin layer of small nanoparticles. The microstructures of the NiO-NPs@GNSs were further characterized by TEM technique. The TEM image (Figure 2c) revealed that the NiO nanoparticles were distributed on the surface of GNSs with a size of 3−5 nm in diameter. There were no free NiO nanoparticles isolated from GNSs or vacancy on GNSs. The above observation also revealed that these NiO particles were firmly attached to the GNSs by considering that ultrasonication was used during the preparation of TEM specimen. The HRTEM image of the NiO-NPs@GNSs is shown in Figure 2e. The lattice fringes with *d*-spacing of 0.24 and 0.21 nm can be assigned to the (111) and (200) planes of the cubic NiO. However, when trace amounts of water was introduced in the mixed solvents, SEM image (Figure 1b) showed that a dense nanoflake arrays grew over the entire surface of GNSs with almost perpendicular direction. With a closer examination, the nanosheet constituents were about 100 nm in length and 5−10 nm in thickness. Such an interesting structure was also viewed under TEM (Figure 1d). Consistent with the above SEM analysis, the NiO nanosheets were mostly grown upright with a random orientation on the GNSs support. The HRTEM (Figure 1f) of the NiO-NFAs@GNSs also showed clearly lattice fringes with *d*-spacing of 0.24 and 0.21 nm, the (111) and (200) planes of the cubic NiO as observed in the NiO-NPs@GNSs.

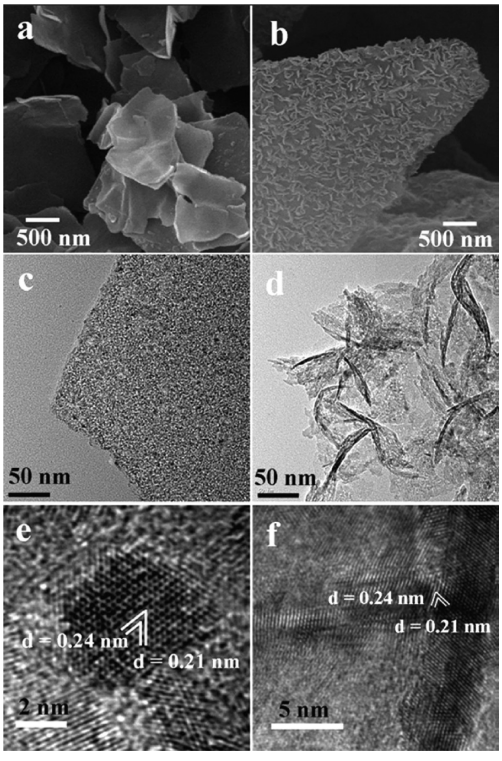

Figure 2. SEM images of (a) NiO-NPs@GNSs and (b) NiO-NFAs@GNSs. TEM images of (c) NiO-NPs@GNSs and (d) NiO-NFAs@GNSs. HRTEM images of (e) NiO-NPs@GNSs and (f) NiO-NFAs@GNSs.

To understand the different growth behaviors of the two distinct NiO nanostructures on GNSs, we performed several experiments to investigate the function of CO_2 and trace amounts of water. At the temperature of 200 °C, nickel nitrate hexahydrate could convert into crystalline solid compounds in pure ethanol without GO and CO_2 whether additional water was added or not. The XRD results (see Figure S3 in the Supporting Information) showed that the compounds were $Ni_3(NO_3)_2(OH)_4$ (JCPDS card 22−0752). SEM images of these compounds exhibited overall thin nanosheet morphologies (see Figure S4 in the Supporting Information). However, when compressed CO_2 was introduced into the vessel, the precursors obtained without or with the presence of additional water showed different chemical structures and compositions. As shown in Figure 3, the Ni-salt had amorphous structure

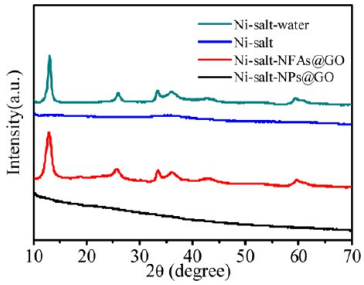

Figure 3. XRD patterns of the Ni-salt-NPs@GO, Ni-salt-NFAs@GO, Ni-salt, and Ni-salt-water.

while the Ni-salt-water had a crystalline structure, which was consistent with the samples synthesized in the presence of GO. The XRD patterns of the Ni-salt-NFAs@GO and Ni-salt-water exhibited typical features for α-phase nickel hydroxide with a general formula ($[Ni(OH)_{2-x}A^{n-}_{x/n}\cdot yH_2O]$ with $x = 0.2-0.4$, $y = 0.6-1$, and A = Cl^-, NO_3^-, SO_4^{2-},CO_3^{2-}, or OCN^-), as reported in the literature. The Ni-salt and Ni-salt-water were also characterized by FTIR spectrum and Elemental analysis. As demonstrated in Figure S5 in the Supporting Information, the interactions of metal ions with NO_3^- and CO_3^{2-} groups were

proved according to the spectrum information of FTIR.[47,48] The new group of CO_3^{2-} should be originated from the reaction of CO_2 and H_2O in this system. Elemental analysis proved that the content of the element of C, H and N in the two precursors was quite different. As shown in Table S1, the content of C in the Ni-salt was higher than that in the Ni-salt-water, whereas the content of N in the Ni-salt was lower than that in the Ni-salt-water. Furthermore, the difference of the content of H between the two precursors was also found. The above results clearly showed that CO_2 and the additional water affected the chemical compositions and structures of the precursors.

Different chemical compositions and structures of the precursors may result different growth behaviors. To investigate the morphologies of the precursors, SEM images were collected for Ni-salt-NPs@GO, Ni-salt-NFAs@GO, Ni-salt, and Ni-salt-water. As shown in panels a and b in Figure 4, the

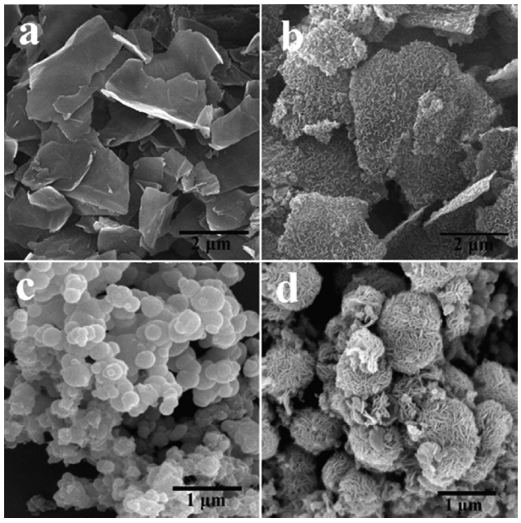

Figure 4. SEM images of the (a) Ni-salt-NPs@GO, (b) Ni-salt-NFAs@GO, (c) Ni-salt, and (d) Ni-salt-water.

morphologies of Ni-salt-NPs@GO and Ni-salt-NFAs@GO were consistent with their calcined ones, which indicated that the morphologies of the precursors were maintained during thermal treatment. Without the presence of GO, the Ni-salt was mainly consisted of particles with the size of 200 nm in diameter (Figure 4c). After trace amounts of water were added during the synthesis, the obtained Ni-salt-water was composed mainly of 3D flowerlike microstructure with the size of 1−2 μm in diameter (Figure 4d). These flowerlike microstructures were assembled mainly of nanosized flakes with the thickness of about 20 nm. From the above results, it was easier to conclude that the additional trace amounts of water played an important role in the conversion of the amorphous precursor to crystalline precursor, which was proposed to be one of the key factors to influence the growth behavior of the precursors on GO. Furthermore, owing to the special properties of $scCO_2$, like the lower viscosity, high mass transfer rate, and absence of surface tension, the metal oxide nanoparticles yielded in the $scCO_2$ tend to deposit onto the surfaces of GO. Meanwhile, $scCO_2$ as an antisolvent reduced the solvent strength caused by hydroxyls originated from ethanol and water, which could lower the aggregation of the final particles.[28,31,49] However, for the pure ethanol, the existence of surface tension, hydroxyls, and low diffusivity, which strongly limit the ability to disperse and transfer of the generated solid intermediates to grow on the surface of substrate, resulted in some NiO particles crystallized and aggregated freely in solution (see Figure S6 in the Supporting Information).

In order to understand the forming process of the 3D flowerlike microstructure, we carried out time-dependent experiments during which samples were collected at different time intervals. As shown in Figure 5a, at the early stage, the

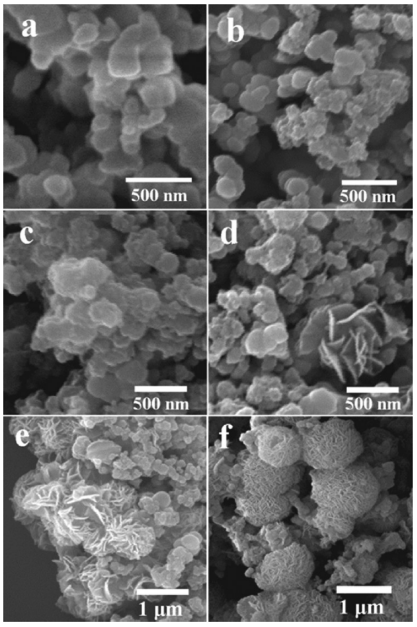

Figure 5. SEM images of the samples formed at different times after the temperature reached 200 °C: (a) 0, (b) 10, (c, d) 30, (e) 50, and (f) 70 min during the formation of 3D flowerlike microstructure.

sample was composed of ca. 200 nm particles. Ten min later, as shown in Figure 5b, some nanoflakes emerged in the sample indicating that anisotropic growth had occurred in this stage. As the reaction proceeded, the amount of nanoflakes increased at the expense of the nanoparticles (Figure 5c). At the same time, 3D microstructure grew gradually and the morphology became flowerlike (Figure 5d). 50 min later, most of the nanoflakes have been assembled to form 3D flowerlike microstructure (Figure 5e). Eventually no nanoflakes remained and the sample was composed entirely of the 3D flowerlike microstructure (Figure 5f). In the forming process, the samples were amorphous at early stage, but the crystallinity of the samples increased when plenty of nanoflakes were formed after 30 min (see Figure S7 in the Supporting Information).

On the basis of above structural and morphological analysis, a possible growth mechanism was proposed as follows. In general, the crystal forming process in a solution is mainly divided into two stages of nucleation and crystal growth, and the special crystal structure and symmetry determine its inherent morphology.[50,51] In the forming process of 3D flowerlike microstructure, the nickel ions were precipitated and nucleated to form amorphous primary particles by hydrolysation and polymerization reactions very quickly at early stage, and then the crystallization of the amorphous primary particles increased gradually as the reaction proceeded. The freshly crystalline seeds were unstable because of their high surface energy and tend to aggregate to form flakes as confirmed by the evidence that the flakes were composed of

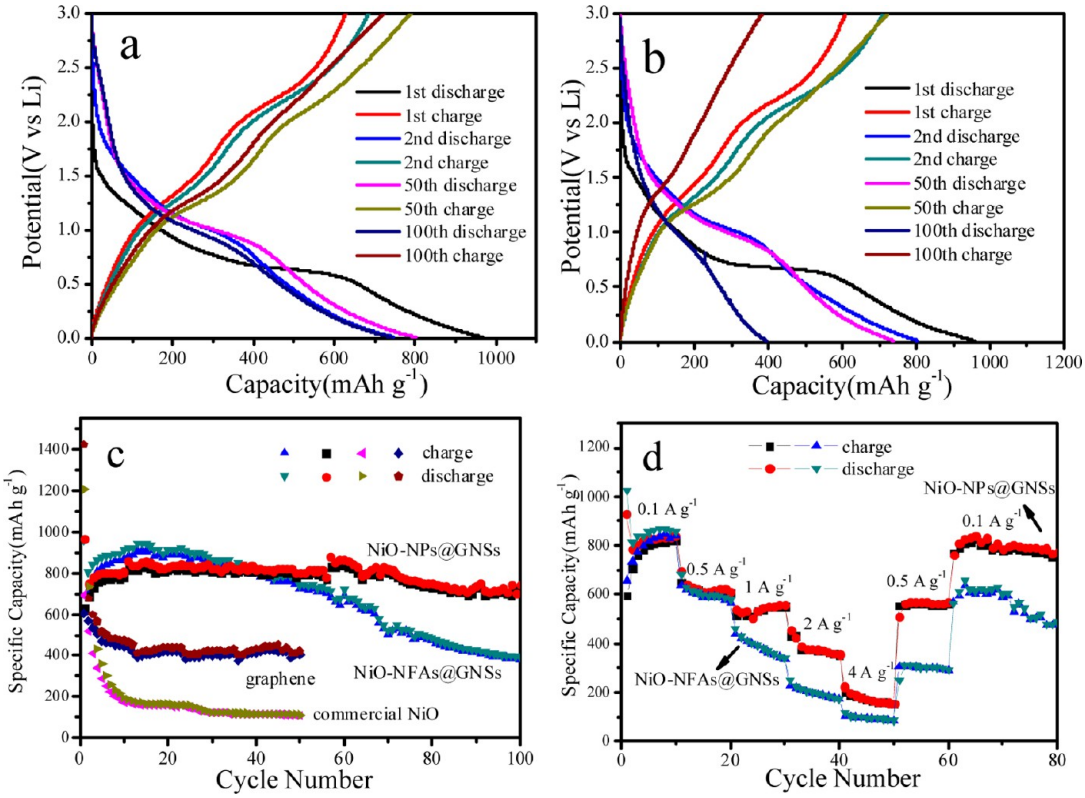

Figure 6. The 1st, 2nd, 50th, and 100th charge−discharge voltage profiles of (a) NiO-NPs@GNSs and (b) NiO-NFAs@GNSs. (c) Cycling performances of the bare GNSs, commercial NiO, NiO-NPs@GNSs, and NiO-NFAs@GNSs at a current of 100 mA g^{-1}. (d) Rate performances of the NiO-NPs@GNSs and NiO-NFAs@GNSs nanocomposites.

nanoparticles (see Figure S8 in the Supporting Information). The assembly of these crystalline seeds to form flakes may be related to the intrinsic lamellar structure of α-$Ni(OH)_2$.[52−54] These nanoflakes took a positive charge because of the hydroxyl defects in the $Ni(OH)_x$ layer originated the intercalation of the special species (water and/or anions) in the interlayer galleries.[54,55] So, the electrostatic and hydrogen bonds might be the main driving forces for self-assembly of nanoflakes into 3D flower microstructure.[54] The growth process is consistent with previous reports of a so-called two-stage growth process, which involves a fast nucleation of amorphous primary particles followed by a slow crystallization and anisotropic growth of primary particles.[56] However, when GO was introduced into the system, the nucleation was preferential on the surface of GO due to the absorption of Ni^{2+} by hydroxyl, carboxyl, or epoxy groups, thus nanoflakes were formed on the surface of GO in situ to form Ni-salt-NFAs@GO. So, the self-assembly of these nanoflakes was prohibited since they were held in position by the GO. For the synthesizing of Ni-salt-NPs@GO, Ni^{2+} could be first randomly adsorbed on the surface of GO as a nucleation site, and the residual Ni^{2+} ions in solution took precedence to continuously absorb on the nucleation sites and grew slowly to large particles. Owing to the amorphous structure of these particles, the stage of anisotropic growth was not involved. Finally, the surfaces of GO were covered with small and uniform nanoparticles.

It has been reported that one mole of NiO has the ability to react with two moles of Li ions through the conversion reaction: $NiO + 2Li^+ + 2e \leftrightarrow Li_2O + Ni$. On the basis of this reaction, the theoretical capacity of NiO was calculated to be 718 mA h g^{-1}. In addition, the largest reversible capacity for the GNSs was 603 mA h g^{-1}. So the theoretical capacity of the NiO@GNSs composite was 681 mA h g^{-1} (603 mA h g^{-1} × 0.315 + 718 mA h g^{-1} × 0.685). The electrochemical performances of NiO-NPs@GNSs and NiO-NFAs@GNSs were evaluated by galvanostatic charge−discharge. Figure 6a-b show the first, second, 50th, and 100th charge−discharge voltage profiles of the cells at current rate of 100 mA g^{-1}. In the discharge curves of the first cycle, both the samples exhibited a typical plateau at around 0.7 V, corresponding to the formation of a solid-electrolyte interfacial (SEI) layer and the reaction of NiO with lithium to from amorphous Li_2O and Ni^0.[23] As shown in Figure 6a, the first discharge and charge capacity for NiO-NPs@GNSs composite was 967 mA h g^{-1} and 629 mA h g^{-1}, respectively. The discharge capacity of the composite at the second, 50th and 100th cycle was 747 mA h g^{-1}, 803 mA h g^{-1} and 741 mA h g^{-1}, respectively. The Coulombic efficiency rose from 65.1% at the first cycle to 91.7% at the second cycle and 97.7% at the 100th cycle. By contrast, the NiO-NFAs@GNSs showed inferior performance compared to NiO-NPs@GNSs. As shown in Figure 6b, the first discharge and charge capacity for NiO-NFAs@GNSs composite was 957 mA h g^{-1} and 608 mA h g^{-1}, respectively. The discharge capacity of the composite at the second, 50th and 100th cycle was 805 mA h g^{-1}, 740 mA h g^{-1} and 394 mA h g^{-1}, respectively.

Figure 6c shows a comparison of the charge−discharge cyclic performances for the bare GNSs, commercial NiO, NiO-NPs@GNSs and NiO-NFAs@GNSs composites. The cells were cycled at a current of 100 mA g^{-1}. The bare GNSs had an initial discharge capacity of 1422 mAh g^{-1} and charge capacity of 603 mAh g^{-1} with a Coulombic efficiency of 42.4%, but after 50 cycles, the charge capacity dropped to 407 mAh g^{-1}. For the

commercial NiO, the capacity faded rapidly due to the severe pulverization after 50 cycles. In contrast with the bare GNSs and commercial NiO, the NiO-NPs@GNSs composite showed enhanced capacity and stable recycled capacity up to 100 cycles. However, the capacity for the NiO-NFAs@GNSs composite faded rapidly after 20 cycles. After cycling up to 100 cycles, the remained charge capacity for NiO-NFAs@GNSs composite was only 383.8 mAh g^{-1}, being about 63% of the first reversible capacity. For the two composites, the reversible capacity was slightly increased in the initial several cycles, which was attributed to the gradual activation of electrode in the first stage.

To further investigate the electrochemical performance of the NiO-NPs@GNSs and NiO-NFAs@GNSs composites, the charge−discharge measurements for them were also carried out at various current densities. Figure 6d demonstrates the rate capability of the two composites electrodes from current densities of 0.1−4 A g^{-1} for ten cycles at each current density. At the low current density (0.1 A g^{-1} and 0.5 A g^{-1}), the capacities of the NiO-NPs@GNSs and NiO-NFAs@GNSs composites are comparable. However, at a higher current density of 2 A g^{-1}, the NiO-NPs@GNSs composite was still able to deliver a discharge capacity of 350 mA h g^{-1}, which is much higher than that of NiO-NFAs@GNSs (171 mA h g^{-1}). Even at a high current density of 4 A g^{-1}, the NiO-NPs@GNSs composite was still able to deliver a capacity of 152 mA h g^{-1}; however, the capacity of the NiO-NFAs@GNSs dropped dramatically to 84 mA h g^{-1}. If the current was returned from 4 to 0.5 A g^{-1}, the specific capacity of the NiO-NPs@GNSs could return to 561 mA h g^{-1}, which was much higher than that of NiO-NFAs@GNSs (289 mA h g^{-1}).

To understand the good electrochemical performance of the NiO-NPs@GNSs, the morphology and microstructure variation in the NiO-NPs@GNSs and NiO-NFAs@GNSs nanocomposites after 100 discharge−charge cycles were examined using XPS, SEM, and TEM. As the XPS spectra of Ni 2p shown in Figure S9 in the Supporting Information, it can be seen that the peaks of the materials after cycling could be well indexed to Ni^0 and oxidized Ni. The small portion of Ni^0 in the cycled samples was probably ascribed to the irreversible reaction in the cells. The SEM (Figure 7a) and TEM images (Figure 7c, e) showed that the size of the NiO particles was almost the same as in the initial state for the NiO-NPs@GNSs nanocomposite after 100 cycles. The spherelike morphology of the NiO nanoparticles which was different from their initial irregular morphology indicated that these particles were suffered from lithiation-delithiation repeatedly. However, the NiO nanoparticles were still closely enbedded in GNSs and no obvious aggregation was observed despite that they had undergone 100 times of volume expansion−contraction associated with the lithium insertion and extraction process, highlighting the structure stability of NiO-NPs@GNSs hybrid electrode. The fact that the NiO particles in the NiO-NPs@GNSs composite did not exhibit agglomeration or size variation should be benefited of the intimate contact of GNSs and the small NiO nanoparticles, which consequently enhanced the cyclic stability and rate capability. However, for the NiO-NFAs@GNSs, due to the small contact interface and little linkage sites of these nanoflake arrays with perpendicular direction, the NiO nanoflakes on the surfaces of GNSs had collapsed and overlapped after 100 cycles (Figure 7b). The TEM images (Figure 7d, f) showed that most of the NiO-NFAs on the surfaces of GNSs had cracked and aggregated into large particles, indicating that the pulverization of the particles in cycling, which leaded to the poor cycling stability of NiO-NFAs@GNSs nanocomposite.

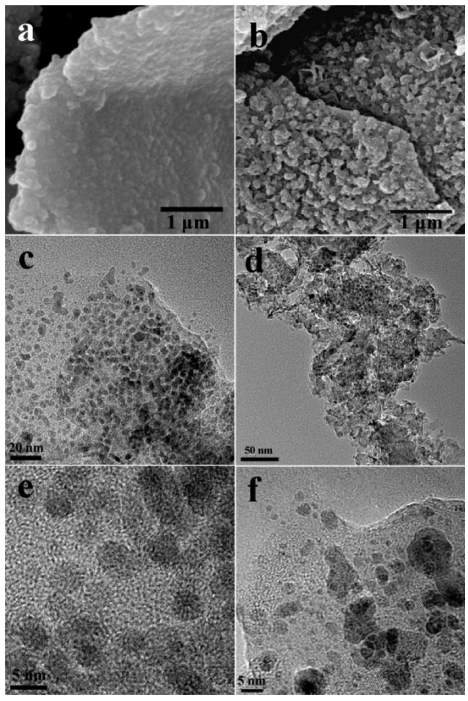

Figure 7. SEM images of the samples after 100 cycles: (a) NiO-NPs@GNSs and (b) NiO-NFAs@GNSs. TEM images of the samples after 100 cycles: (c, e) NiO-NPs@GNSs and (d, f) NiO-NFAs@GNSs.

4. CONCLUSIONS

In summary, we have developed a new method to grow NiO nanomaterials on GNSs through a simple low temperature chemical deposition in CE. The morphologies of NiO nanomaterials grown on GNSs could be tailored by trace amounts of water introduced in CE. Small and uniform nanoparticles of NiO were covered on the surfaces of GNSs through the decomposition of nickel nitrate in CE directly. However, when trace amounts of water was introduced into the mixed solvents, NiO nanoflake arrays were grown on the surface of GNSs. The quiet different chemical compositions and structures of the two formed precursors were proposed to be the key factors to influence the growth behaviors of the two distinct nanostructures on the surface of GNSs. When used as anode material for LIBs, the NiO-NPs@GNSs composite exhibited a higher reversible capacity, better cycle and rate performance compared with the NiO-NFAs@GNSs. At a higher current densities of 2 and 4 A g^{-1}, the NiO-NPs@GNSs composite could deliver a discharge capacity of 350 and 152 mA h g^{-1}, respectively, which was much higher than that of NiO-NFAs@GNSs (171 mA h g^{-1} and 85 mA h g^{-1}). If the current was returned from 4 A g^{-1} to 0.5 A g^{-1}, the specific capacity of the NiO-NPs@GNSs could still return to 561 mAh g^{-1}. The better electrochemical performances of the NiO-NPs@GNSs composite was benefited of the intimate contact of GNSs and the small NiO nanoparticles, resulting in the NiO-NPs keeping well dispersion without any agglomeration or size variation after 100 times recycling. Because the presented method does not need tedious pretreatment, surfactants, high viscous solvents, and precipitate, it is a green technology, which

could be easily extended to the synthesis of a wide range of functional nanomaterials.

■ ASSOCIATED CONTENT

Supporting Information

Figures S1−S9. This material is available free of charge via the Internet at http://pubs.acs.org/.

■ AUTHOR INFORMATION

Corresponding Author

*E-mail: xbzhang@ciac.jl.cn (X.Z.); Zhaofy@ciac.jl.cn (F.Z.). Tel and Fax: +86-431-85262410.

Notes

The authors declare no competing financial interest.

■ ACKNOWLEDGMENTS

This work was financially supported by the One Hundred Talent Program of CAS and NSFC (21273222).

■ REFERENCES

(1) Wang, H. L.; Robinson, J. T.; Diankov, G.; Dai, H. J. *J. Am. Chem. Soc.* **2010**, *132*, 3270−3271.
(2) Wang, H. L.; Cui, L. F.; Yang, Y. A.; Casalongue, H. S.; Robinson, J. T.; Liang, Y. Y.; Cui, Y.; Dai, H. J. *J. Am. Chem. Soc.* **2010**, *132*, 13978−13980.
(3) Wang, H. L.; Casalongue, H. S.; Liang, Y. Y.; Dai, H. J. *J. Am. Chem. Soc.* **2010**, *132*, 7472−7477.
(4) Li, L.; Wang, T. T.; Zhang, L. Y.; Su, Z. M.; Wang, C. G.; Wang, R. S. *Chem.—Eur. J.* **2012**, *18*, 11417−11422.
(5) Zhou, G. M.; Wang, D. W.; Li, F.; Zhang, L. L.; Li, N.; Wu, Z. S.; Wen, L.; Lu, G. Q.; Cheng, H. M. *Chem. Mater.* **2010**, *22*, 5306−5313.
(6) Xia, X. H.; Tu, J. P.; Mai, Y. J.; Chen, R.; Wang, X. L.; Gu, C. D.; Zhao, X. B. *Chem.—Eur. J.* **2011**, *17*, 10898−10905.
(7) Zhu, X. J.; Zhu, Y. W.; Murali, S.; Stollers, M. D.; Ruoff, R. S. *ACS Nano* **2011**, *5*, 3333−3338.
(8) Zhou, G. M.; Wang, D. W.; Yin, L. C.; Li, N.; Li, F.; Cheng, H. M. *ACS Nano* **2012**, *6*, 3214−3223.
(9) Gu, Y.; Xu, Y.; Wang, Y. *ACS Appl. Mater. Interfaces* **2013**, *5*, 801−806.
(10) Zhu, X. J.; Dai, H. L.; Hu, J.; Ding, L.; Jiang, L. *J. Power Sources* **2012**, *203*, 243−249.
(11) Qi, Y.; Zhang, H.; Du, N.; Yang, D. R. *J. Mater. Chem. A* **2013**, *1*, 2337−2342.
(12) Wang, G. X.; Wang, B.; Wang, X. L.; Park, J.; Dou, S. X.; Ahn, H.; Kim, K. *J. Mater. Chem.* **2009**, *19*, 8378−8384.
(13) Liang, J. F.; Wei, W.; Zhong, D.; Yang, Q. L.; Li, L. D.; Guo, L. *ACS Appl. Mater. Interfaces* **2012**, *4*, 454−459.
(14) Zhou, X. S.; Yin, Y. X.; Cao, A. M.; Wan, L. J.; Guo, Y. G. *ACS Appl. Mater. Interfaces* **2012**, *4*, 2824−2828.
(15) Ding, S.; Luan, D.; Boey, F. Y.; Chen, J. S.; Lou, X. W. *Chem. Commun.* **2011**, *47*, 7155−7157.
(16) Choi, J.; Jin, J.; Jung, I. G.; Kim, J. M.; Kim, H. J.; Son, S. U. *Chem. Commun.* **2011**, *47*, 5241−5243.
(17) Wang, J. Z.; Zhong, C.; Wexler, D.; Idris, N. H.; Wang, Z. X.; Chen, L. Q.; Liu, H. K. *Chem.—Eur. J.* **2011**, *17*, 661−667.
(18) Vinayan, B. P.; Ramaprabhu, S. *J. Mater. Chem. A* **2013**, *1*, 3865−3871.
(19) Qiu, J. X.; Zhang, P.; Ling, M.; Li, S.; Liu, P. R.; Zhao, H. J.; Zhang, S. Q. *ACS Appl. Mater. Interfaces* **2012**, *4*, 3636−3642.
(20) Chang, K.; Chen, W. X. *ACS Nano* **2011**, *5*, 4720−4278.
(21) Luo, B.; Fang, Y.; Wang, B.; Zhou, J.; Song, H.; Zhi, L. *Energy Environ. Sci.* **2012**, *5*, 5226−5230.
(22) He, Y. S.; Bai, D. W.; Yang, X.; Chen, J.; Liao, X. Z.; Ma, Z. F. *Electrochem. Commun.* **2010**, *12*, 570−573.
(23) Zou, Y. Q.; Wang, Y. *Nanoscale* **2011**, *3*, 2615−2620.
(24) Chen, S.; Zhu, J. W.; Wu, X. D.; Han, Q. F.; Wang, X. *ACS Nano* **2010**, *4*, 2822−2830.
(25) Wu, Z. S.; Ren, W.; Wang, D. W.; Li, F.; Liu, B.; Cheng, H. M. *ACS Nano* **2010**, *4*, 5835−5842.
(26) Xu, C. H.; Sun, J.; Gao, L. *Nanoscale* **2012**, *4*, 5425−5430.
(27) Eckert, C. A.; Knutson, B. L.; Debenedetti, P. G. *Nature* **1996**, *383*, 313−318.
(28) Pessey, V.; Garriga, R.; Weill, F.; Chevalier, B.; Etourneau, J.; Cansell, F. *J. Mater. Chem.* **2002**, *12*, 958−965.
(29) Ming, J.; Cheng, H. Y.; Yu, Y. C.; Wu, Y. Q.; Zhao, F. Y. *J. Mater. Chem.* **2011**, *21*, 6654−6659.
(30) Cansell, F.; Aymonier, C. *J. Supercrit. Fluids* **2009**, *47*, 508−516.
(31) Liu, Z.; Han, B. *Adv. Mater.* **2009**, *21*, 825−829.
(32) Fu, L.; Liu, Z. M.; Liu, Y. Q.; Han, B. X.; Wang, J. Q.; Hu, P. G.; Cao, L. C.; Zhu, D. B. *Adv. Mater.* **2004**, *16*, 350−352.
(33) Wu, H.; Xu, M.; Wu, H.; Xu, J.; Wang, Y.; Peng, Z.; Zheng, G. *J. Mater. Chem.* **2012**, *22*, 19821−19825.
(34) Tao, L. Q.; Zai, J. T.; Wang, K. X.; Wan, Y. H.; Zhang, H. J.; Yu, C.; Xiao, Y. L.; Qian, X. F. *RSC Adv.* **2012**, *2*, 3410−3415.
(35) Mai, Y. J.; Tu, J. P.; Gu, C. D.; Wang, X. L. *J. Power Sources* **2012**, *209*, 1−6.
(36) Mai, Y. J.; Shi, S. J.; Zhang, D.; Lu, Y.; Gu, C. D.; Tu, J. P. *J. Power Sources* **2012**, *204*, 155−161.
(37) Huang, Y.; Huang, X. L.; Lian, J. S.; Xu, D.; Wang, L. M.; Zhang, X. B. *J. Mater. Chem.* **2012**, *22*, 2844−2847.
(38) Liu, H.; Wang, G. X.; Liu, J. A.; Qiao, S. Z.; Ahn, H. J. *J. Mater. Chem.* **2011**, *21*, 3046−3052.
(39) Zhang, G. H.; Chen, Y. J.; Qu, B. H.; Hu, L. L.; Mei, L.; Lei, D. N.; Li, Q.; Chen, L. B.; Li, Q. H.; Wang, T. H. *Electrochim. Acta* **2012**, *80*, 140−147.
(40) Xia, Y.; Zhang, W.; Xiao, Z.; Huang, H.; Zeng, H.; Chen, X.; Chen, F.; Gan, Y.; Tao, X. *J. Mater. Chem.* **2012**, *22*, 9209−9215.
(41) Qiu, D. F.; Xu, Z. J.; Zheng, M. B.; Zhao, B.; Pan, L. J.; Pu, L.; Shi, Y. *J. Solid State Electrochem.* **2012**, *16*, 1889−1892.
(42) Lu, L.; Yan, X.; Wang, J.; Zheng, H.; Hu, X.; Tang, Y.; Jia, Z. *J. Phys. Chem. C* **2012**, *116*, 14638−14643.
(43) Zhang, G. Q.; Yu, L.; Hoster, H. E.; Lou, X. W. *Nanoscale* **2013**, *5*, 877−881.
(44) Li, J. T.; Zhao, W.; Huang, F. Q.; Manivannan, A.; Wu, N. Q. *Nanoscale* **2011**, *3*, 5103−5109.
(45) Wen, W.; Wu, J. M.; Cao, M. H. *J. Mater. Chem. A* **2013**, *1*, 3881−3885.
(46) Zhu, Y. G.; Cao, G. S.; Xie, J.; Zhu, T. J.; Zhao, X. B. *Nanosci. Nanotechnol. Lett.* **2012**, *4*, 35−40.
(47) Hu, J. C.; Zhu, K. K.; Chen, L. F.; Yang, H. J.; Li, Z.; Suchopar, A.; Richards, R. *Adv. Mater.* **2008**, *20*, 267−271.
(48) Ming, J.; Wu, C. Y.; Cheng, H. Y.; Yu, Y. C.; Zhao, F. Y. *J. Supercrit. Fluids* **2011**, *57*, 137−142.
(49) Sun, Z.; Zhang, X.; Han, B.; Wu, Y.; An, G.; Liu, Z.; Miao, S.; Miao, Z. *Carbon* **2007**, *45*, 2589−2596.
(50) Peng, Z. A.; Peng, X. *J. Am. Chem. Soc.* **2002**, *124*, 3343−3353.
(51) Wang, L.; Zhao, Y.; Lai, Q.; Hao, Y. *J. Alloys Compd.* **2010**, *495*, 82−87.
(52) Jeevanandam, P.; Koltypin, Y.; Gedanken, A. *Nano Lett.* **2001**, *1*, 263−266.
(53) Wang, H.; Gao, J.; Li, Z.; Ge, Y.; Kan, K.; Shi, K. *CrystEngComm* **2012**, *14*, 6843−6852.
(54) Xu, L.; Ding, Y.-S.; Chen, C.-H.; Zhao, L.; Rimkus, C.; Joesten, R.; Suib, S. L. *Chem. Mater.* **2007**, *20*, 308−316.
(55) Lee, J. W.; Ko, J. M.; Kim, J.-D. *J. Phys. Chem. C* **2011**, *115*, 19445−19454.
(56) Zhong, L. S.; Hu, J. S.; Liang, H. P.; Cao, A. M.; Song, W. G.; Wan, L. J. *Adv. Mater.* **2006**, *18*, 2426−2431.